

## Electropumping of water with rotating electric fields

Sergio De Luca,<sup>1</sup> B. D. Todd,<sup>1,a)</sup> J. S. Hansen,<sup>2</sup> and Peter J. Daivis<sup>3</sup>

<sup>1</sup>*Mathematics, Faculty of Engineering and Industrial Sciences, and Centre for Molecular Simulation, Swinburne University of Technology, Melbourne, Victoria 3122, Australia*

<sup>2</sup>*DNRF Center "Glass and Time," IMFUFA, Department of Science, Systems and Models, Roskilde University, DK-4000 Roskilde, Denmark*

<sup>3</sup>*School of Applied Sciences, RMIT University, Melbourne, Victoria 3001, Australia*

(Received 27 November 2012; accepted 18 March 2013; published online 19 April 2013)

Pumping of fluids confined to nanometer dimension spaces is a technically challenging yet vitally important technological application with far reaching consequences for lab-on-a-chip devices, biomimetic nanoscale reactors, nanoscale filtration devices and the like. All current pumping mechanisms require some sort of direct intrusion into the nanofluidic system, and involve mechanical or electronic components. In this paper, we present the first nonequilibrium molecular dynamics results to demonstrate that non-intrusive electropumping of liquid water on the nanoscale can be performed by subtly exploiting the coupling of spin angular momentum to linear streaming momentum. A spatially uniform rotating electric field is applied to water molecules, which couples to their permanent electric dipole moments. The resulting molecular rotational momentum is converted into linear streaming momentum of the fluid. By selectively tuning the degree of hydrophobicity of the solid walls one can generate a net unidirectional flow. Our results for the linear streaming and angular velocities of the confined water are in general agreement with the extended hydrodynamical theory for this process, though also suggest refinements to the theory are required. These numerical experiments confirm that this new concept for pumping of polar nanofluids can be employed under laboratory conditions, opening up significant new technological possibilities.

© 2013 AIP Publishing LLC. [<http://dx.doi.org/10.1063/1.4801033>]

### I. INTRODUCTION

As modern devices continue to shrink, the application of nanofluidic circuitry to useful functioning devices remains a significant challenge. Pumping small volumes of fluid is a significant problem, largely because applications in technologies such as lab-on-a-chip devices for DNA analysis, biomimetic nanoscale reactors and networks, and desalination science all require some form of nanoscale pumping technology.<sup>1-3</sup> However, mechanical pumping at the nanoscale is difficult due to the scale limitations of miniaturisation of mechanical pumps. There are several existing methods with varying degrees of success, including electro-osmotic (or electrokinetic) flow (EOF).<sup>4,5</sup> The EOF is widely used in chemical separation technologies such as capillary electrophoresis, but is also used in microfluidic devices<sup>4,6</sup> with a particularly important application to lab-on-a-chip devices. However, it is limited to ionic fluids.

For non-ionic fluids mechanical pumping is generally required, in which a pressure differential is applied. However, this involves very large pressure gradients due to the large hydrostatic resistance of nanochannels, which in turn invokes other serious technical challenges.<sup>4</sup> Alternative means of pumping involve combinations of electric, magnetic or mechanical forces,<sup>7-13</sup> or time-dependent electric fields.<sup>14</sup>

All these pumping mechanisms involve intrusive access into the nanofluidic circuitry itself. Either the electrodes need

to be physically attached to nano-conduits, or some other form of mechanical pumping device must be attached. This causes technical difficulties and increases the size of the nanofluidic device. Pumping that involves no physical intrusion into the nanofluidic circuitry is an obvious advantage and would amount to a milestone in nanotechnology. In this paper, we demonstrate such a mechanism via molecular dynamics computer experiments and extended Navier-Stokes hydrodynamics theory.

Our approach is based upon three insights gained from recent theoretical studies:<sup>15,17-23</sup> (1) Linear and angular momentum of molecularly structured fluids can couple effectively, thus allowing a mechanism for the exchange of streaming and angular velocity;<sup>15,17,18,21,22,24</sup> (2) the boundary conditions themselves play a significant role in nanofluidic flow. Confining a fluid between walls that are not composed of the same material, in which one wall is hydrophilic while the other is hydrophobic, destroys the symmetry of slip boundary conditions, which in turn ensures a non-zero net flow; and (3) the application of a rotating electric field can cause a polar molecule to spin, and when under extreme confinement this spin angular momentum can be efficiently converted into linear streaming flow.<sup>15,18</sup> If the wall surfaces consist of the same material, there is equal flow in both directions but no net flow; however, if the walls consist of different materials with significantly different degrees of hydrophobicity, a net linear translational flow can be generated.

In what follows we present results of the first nonequilibrium molecular dynamics (NEMD) computer experiments for

<sup>a)</sup>Electronic mail: btodd@swin.edu.au

a system of water molecules under the influence of a spatially uniform rotating electric field confined to a nano-channel. Our simulations demonstrate that this coupling between rotational and translational molecular motion can be applied to pump nanoscale fluids under experimentally accessible laboratory conditions and opens the possibility of a new method for fluid actuation involving no physical intrusion in the nanofluidic circuitry itself.

## II. SIMULATIONS

All nonequilibrium molecular dynamics computer experiments were performed using code developed by the authors. Our NEMD simulation systems consist of water molecules confined between two different planar solid atomistic surfaces: one hydrophobic and one hydrophilic. We model liquid water using the SPC/E pair potential,<sup>25,26</sup> chosen for its good reproduction of experimental viscosity coefficients. The hydrogen site has a partial charge of  $q_H = 0.4238e$  while  $q_O = -0.8476e$  for oxygen ( $e = 1.6 \times 10^{-19}$  C is the fundamental unit of charge). Water bonds were constrained using the SHAKE algorithm,<sup>27</sup> with the O–H bond length and H–O–H angle fixed at 0.1 nm and  $109.5^\circ$ , respectively. Hence, the dipole moment of SPC/E water is 2.35 D, which is within error estimates of the experimental value of  $2.9 \pm 0.6$  D.<sup>28</sup>

The system volume consists of a rectangular box of dimensions  $L_x = 1.899$  nm,  $L_y = 4.481$  nm, and  $L_z = 1.899$  nm, periodic in the  $x$  and  $z$  directions.

Water molecules interact through a pairwise additive Lennard-Jones (LJ) potential and a Coulomb potential given by

$$\phi = \sum_i \sum_{j>i} 4\epsilon \left[ \left( \frac{\sigma}{r_{ij}} \right)^{12} - \left( \frac{\sigma}{r_{ij}} \right)^6 \right] + \sum_i \sum_{j>i} \frac{q_i q_j}{r_{ij}}, \quad (1)$$

where the LJ parameters  $\epsilon$  and  $\sigma$  are the energy and length scale parameters and  $r_{ij} = |\mathbf{r}_i - \mathbf{r}_j|$  is the distance between O–O, O–H, and H–H atoms of different water molecules, as well as the distance between water site charges and charged wall atoms. The LJ potential for the water-water interactions is truncated at  $r = 2.5\sigma$ . In this study, we have used as characteristic dimensions  $\sigma = 0.3166$  nm,  $\epsilon = 0.6502$  kJ mol<sup>-1</sup> (LJ parameters of the SPC/E model) and  $m_O = 16$  amu as length, energy, and mass scaling factors. The density of the water was  $\rho = 998$  kg m<sup>-3</sup> which, after fixing the fluid volume in the simulation box, yields a total number of water molecules  $N = 270$ .

To bring the system out of equilibrium we use a spatially uniform rotating electric field, polarized in the  $x$ - $y$  plane (see Fig. 1). The field can be represented as  $\mathbf{E} = E(\cos(\omega t), \sin(\omega t), 0)$ , where  $E$  is the amplitude of the

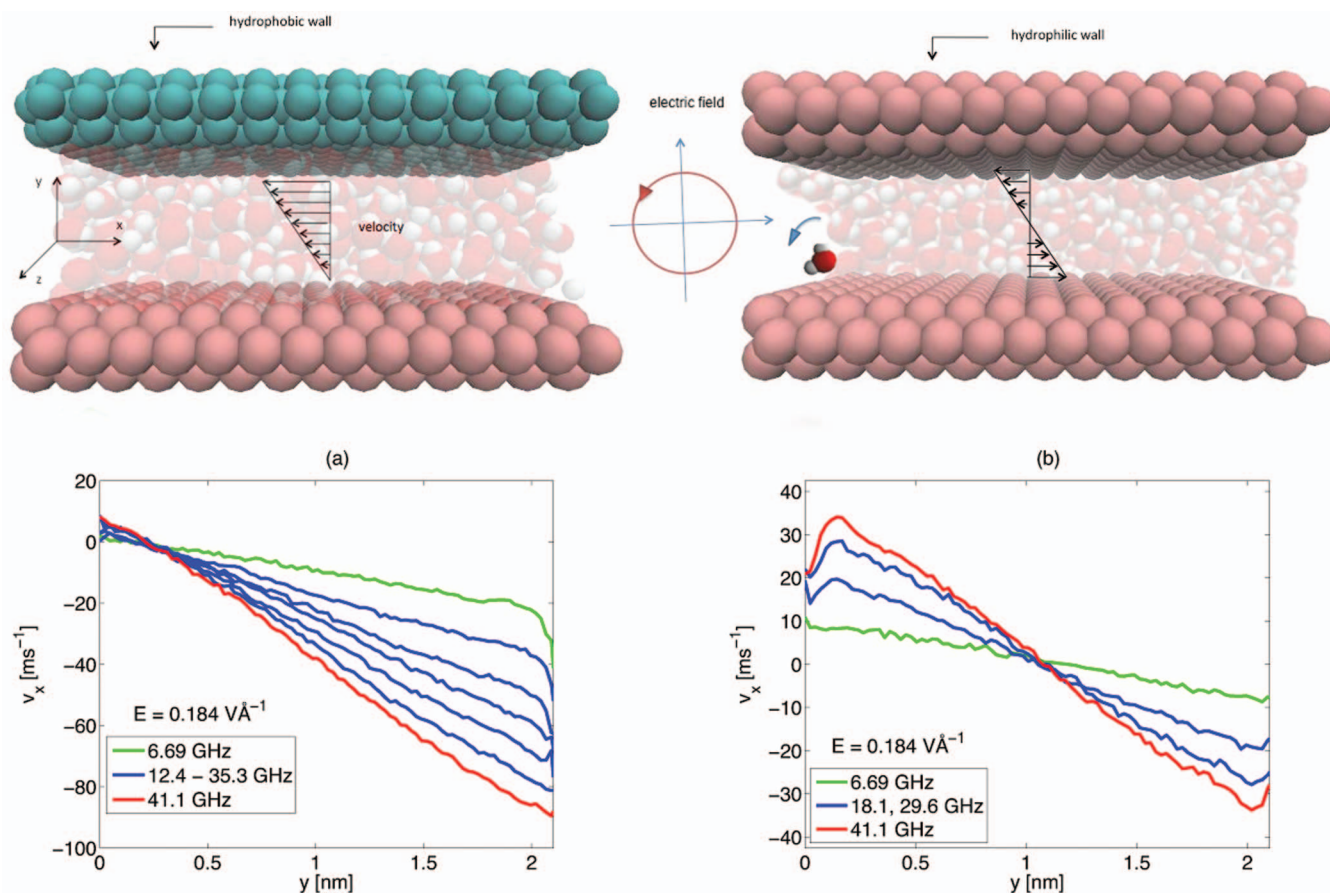


FIG. 1. System configuration and streaming velocity profiles. (a) The lower surface (pink) represents the hydrophilic wall while the upper wall is hydrophobic. Streaming velocity profiles are shown below, where the horizontal axis gives the  $y$ -coordinate in the channel. The amplitude of the external field is fixed while the frequency varies in steps of approximately 6 GHz. (b) Two hydrophilic walls and the associated streaming velocity profiles at fixed field strength and variable frequency. Images generated using VMD.<sup>50</sup>

electric field and  $\omega/2\pi$  is the frequency. Therefore, the total torque acting on a single molecule is

$$\boldsymbol{\tau} = \sum_i (\mathbf{r}_i - \mathbf{r}_{cm}) \times q_i \mathbf{E}_i, \quad (2)$$

where the sum is over the 3 atomic sites of water molecules and  $q_i$  are the partial charges on the oxygen and hydrogen atoms. Inducing this torque results in water molecules attempting to reorient their permanent dipole  $\boldsymbol{\mu}$  along the field, resulting in an axis of rotation parallel to the  $z$  axis.

In this study the magnitude of the electric field ranges from  $7.89 \times 10^{-2} \text{ V \AA}^{-1}$  to  $0.237 \text{ V \AA}^{-1}$ , with frequencies taken in a small window of the microwave region, 6.69–41.1 GHz. To put these values into perspective, we note that a large heating of water<sup>29</sup> is attainable with a microwave electric field of 100 GHz and  $0.1 \text{ V \AA}^{-1}$ .

To break the spatial symmetry of the channel, we implement one hydrophilic and one hydrophobic wall, simulating no-slip and slip boundary conditions, respectively. To obtain this effect, we have altered the strength of the LJ potential between water and wall particles. Moreover, we design two different crystalline structures for the surfaces (described below). To maximize the slip length on the hydrophobic wall, we represent the interactions between water and wall particles with the Weeks-Chandler-Andersen (WCA) potential,<sup>30</sup> a purely repulsive LJ potential truncated at its minimum  $r_c = 2^{1/6}\sigma$  and shifted to zero at the cutoff distance. The LJ parameters are set to  $\sigma_{wall} = 0.158 \text{ nm}$  and  $\epsilon_{wall} = 0.2923 \text{ kJ mol}^{-1}$ , a value less than half  $\epsilon_{SPC/E}$ . To further enhance the slip length, we choose for the density of the hydrophobic wall a value approximately two times larger than the hydrophilic wall density, such that water molecules experience a smoother potential energy landscape when interacting with this wall. We design the hydrophilic wall on the opposite side of the channel such that its properties are tuned to approximately reproduce the stick boundary condition (zero velocity slip length). A schematic diagram of the system under investigation is shown in Fig. 1.

The two planar walls were positioned parallel to the  $x$ - $z$  directions. The centre of mass of the two innermost atomic planes is separated by a distance of 2.5 nm in the  $y$ -direction. The interaction between the hydrophilic wall particles and water molecules is the same LJ potential used for water-water interactions, truncated at  $r = 2.5\sigma$ . This tuning guarantees a sufficient degree of hydrophilicity. This was further enforced by distributing charges on the innermost hydrophilic plate. Atoms are given charges with  $q = \pm 0.004e$  placed in an alternating fashion to ensure overall charge neutrality. Note that the wall atoms themselves only interact with each other via the Lennard-Jones potential and not with Coulomb interactions.

Each solid wall was constructed using three layers of atoms in such a manner that the thickness in the  $y$ -direction was identical for the two types of solid walls. The hydrophobic wall is given an FCC (face-centered-cubic) crystal structure, with unit cell length 0.3166 nm, resulting in a total of 216 atoms, with each wall layer having 72 atoms with the crystal plane (111) in contact with the liquid. The hydrophilic wall is modeled by a BCC (body-centered-cubic) structure,

with the same unit cell length, for a total of 108 atoms. The atomic weight for all wall particles is set to 16 amu (same as oxygen). Hence, we obtain a density  $\sim 3.3 \text{ g cm}^{-3}$  for the hydrophobic wall and  $\sim 1.7 \text{ g cm}^{-3}$  for the hydrophilic one. The effective channel width,  $h$ , is thus defined as the distance between the centres of mass of the two innermost atomic wall planes less the sum of effective interatomic radii of the hydrophobic and hydrophilic wall atoms, i.e.,  $h = 2.5 - (\sigma_1 + \sigma_2)/2 \approx 2.5 - (0.158 + 0.316)/2 \sim 2.25 \text{ nm}$ , where  $\sigma_1$  and  $\sigma_2$  are the values of  $\sigma_{wall}$  for the hydrophobic and hydrophilic walls, respectively.

All wall atoms are bound to their equilibrium lattice positions  $\mathbf{r}_{i0}$  by subjecting them to an elastic force

$$\mathbf{F}_{e,i} = -k(\mathbf{r}_i - \mathbf{r}_{i0}), \quad (3)$$

where  $k = 3.234 \text{ Nm}^{-1}$  is the wall spring constant, and  $\mathbf{r}_i$  represents the center of mass position of a wall particle. The long ranged electrostatic interactions have been treated by the Wolf method,<sup>31</sup> and spherically truncated at 0.918 nm, for both water-water and water-wall interactions. The Wolf method is known to induce a fictitious electric field in confined systems.<sup>32</sup> However, we have checked that for our system this effect is small compared to the large applied electric field (around 1%) and can be safely ignored.

The inclusion of an external electric field into the fluid system leads to a body force term in the Newtonian equations of motion for the fluid system:

$$\dot{\mathbf{r}}_i = \frac{\mathbf{p}_i}{m_i}, \quad (4)$$

$$\dot{\mathbf{p}}_i = \mathbf{F}_i + q_i \mathbf{E}_i(t), \quad (5)$$

where  $m_i$  is the mass of atom  $i$ ,  $q_i$  is its charge,  $\mathbf{p}_i$  is the laboratory momentum of atom  $i$ ,  $\mathbf{F}_i(t)$  represents the total intermolecular force acting on atom  $i$  due to all other atoms, and  $\mathbf{E}_i(t)$  is the time-dependent external field acting on atom  $i$ . We set the amplitude of the electric fields such that a significant fluid velocity is achievable in the accessible simulation time of  $\sim 10 \text{ ns}$ , with a concomitant low or moderate heating of water. To address both requirements we found an adequate frequency range around  $\omega/2\pi = 6\text{--}41 \text{ GHz}$ , with electric field amplitude  $\sim 0.1 \text{ V \AA}^{-1}$ . In view of the results shown in Sec. III, we remark that we chose the lowest possible frequency values that result in a significant net flow rate production (to be explained in Sec. III). In this case, even if the water dipole is able to follow the field during each cycle, the number of cycles per second is relatively low and so too is the energy dissipation.

The equations of motion for all particles were integrated using a leap-frog integration scheme,<sup>33</sup> with a time step  $\Delta t = 1.57 \text{ fs}$ . We note that for the wall atoms, Eq. (5) is modified so that the external electric field term is removed, an elastic spring force is included in the form of Eq. (3) and a Nosé-Hoover thermostat term<sup>34–36</sup> is included to extract heat from the walls and keep the fluid temperature approximately constant at the wall temperature of  $T_w = 300\text{K}$  for the lowest flow rates, as we will see later. This is a more accurate means to model a real experimental situation, in which the excess heat generated in the fluid will conduct through the

walls, because it avoids unphysical complications that do arise when artificially thermostating the fluid in highly confined geometries.<sup>37</sup> A further benefit is to leave the rotational and translational dynamics of water unaffected by the velocity thermostating.<sup>38–40</sup>

Note that the value of the wall spring constant has an influence not only on the efficiency by which the thermostat removes heat from the fluid, but also on the amount of slip between water and wall.<sup>41</sup> Nonetheless, we choose to use the same spring constant value for both the hydrophobic and hydrophilic surface, to have a more homogeneous conduction of heat from the two sides of the channel.

Before commencing the simulations, water molecules are first distributed on a grid such that oxygen atoms are separated by  $\sigma = 0.27$  nm and hence do not overlap. For the first 5000 time steps the fluid temperature was adjusted through a direct rescaling of fluid particle velocities. After this initial simulation phase, the Nosé-Hoover thermostat was applied only to the wall particles. This allowed for a faster equilibration time. Finally, after 300 ps we switched on the rotating field and allowed the system to attain steady-state (typically around 6 ns) before accumulating time averages of quantities of interest. Averages of dynamical quantities were collected by applying standard binning techniques,<sup>42</sup> with 200 bins of size  $\Delta y = 0.02$  nm, sampling every 10 time steps for around 7 ns per simulation run.

The streaming velocity  $v_x(y)$  is plotted against channel position (normal to the wall surfaces, i.e., the  $y$ -direction) and has been computed from the microscopic definition of the momentum flux density

$$J_x(\mathbf{r}, t) = \sum_i m_i v_{x,i} \delta(\mathbf{r} - \mathbf{r}_i) \quad (6)$$

divided by the mass density

$$\rho = \sum_i m_i \delta(\mathbf{r} - \mathbf{r}_i), \quad (7)$$

where here  $i$  indexes molecule  $i$ ,  $m_i$  is the mass of water molecule  $i$ ,  $v_{x,i}$  is the  $x$ -velocity component of the  $i$ -th water molecule averaged over the  $x$  and  $z$  coordinates and  $\mathbf{r}_i$  is the center of mass of molecule  $i$ . For every slab, localized between  $y$  and  $y + \Delta y$ , the streaming velocity is computed at the end of each simulation run as

$$v_x(y) = \frac{\langle \sum_i m_i v_{x,i} \delta(y_i - y) \rangle}{\langle \sum_i m_i \delta(y_i - y) \rangle}, \quad (8)$$

where the angle brackets imply time averages.

### III. RESULTS

In Fig. 1 we show a schematic of the simulation system, in which water molecules are confined by atomistic walls separated by nanometer distances. In Fig. 1(a) one wall is hydrophobic and the other hydrophilic, whereas in Fig. 1(b) both walls are hydrophilic. Also plotted in Figs. 1(a) and 1(b) are the linear streaming velocity profiles that are generated when both systems are subjected to a rotating electric field. The small regions immediately adjacent to the walls are excluded due to large statistical error caused by volume exclusion in

these density depleted regions of fluid (see further details at the end of this section on the density profile and former details on the streaming velocity profile estimate).

Figure 1(a) shows the results of seven independent runs performed for the channel width  $h = 2.25$  nm and  $N = 270$  water molecules. The field frequency ranged from  $\omega/2\pi = 6.69$  GHz (green curve) to 41.1 GHz (red curve) while the amplitude was held fixed at  $E = 0.184$  V Å<sup>-1</sup>. Blue curves represent simulations with intermediate frequencies. For the lowest frequency used (green curve), it can be seen that the maximum streaming velocity is around  $v_x = -20$  ms<sup>-1</sup>, obtained next to the hydrophobic (high slip) wall (ignoring values immediately adjacent to the wall). On the hydrophilic (stick) counterpart an almost vanishing fluid velocity is detected.

Gradually increasing the frequency from  $\omega/2\pi = 6.69$  GHz to 41.1 GHz, the largest value used in this work, results in a monotonic increase of the slope of the velocity profile. Below a frequency of 120 GHz (inverse of the dipolar relaxation time of water), the dipoles are able to follow the field. In our frequency range ( $\leq 40$  GHz) we are in that regime. Consequently, as the number of electric field oscillations per unit time increases (remaining within our frequency range), the coupling between spin angular momentum and linear streaming momentum is enhanced (water rotates more often per unit time). The largest increase in the net flow rate was found for  $\omega/2\pi = 41.1$  GHz, which gives  $v_x \sim -80$  ms<sup>-1</sup>, shown as the red profile in Fig. 1(a). The fact that our simulations find net non-zero flow rates for such a system confirms recent theoretical predictions.<sup>15,18</sup>

Figure 1(b) shows results for the case in which water is confined between two identical hydrophilic surfaces. Results are obtained from four simulations with fixed  $E = 0.184$  V Å<sup>-1</sup>, while varying the frequency over the range  $\omega/2\pi = 6.69$ –41.1 GHz. This is a subset of the frequency range in Fig. 1(a) and with the same field strength. Based on continuum descriptions, theory predicts that in the case of identical walls equal and opposite flow should result, but with a zero net flow.<sup>15,18</sup> Our simulation results confirm this. Even though flow does result, all linear streaming velocities of the water in one half of the channel are exactly equal in magnitude, but opposite in direction, to those in the other half, resulting in a net zero flow rate. We still observe the trend that increasing frequency results in stronger flow in any fixed point in the channel. There could be interesting applications of this phenomenon, perhaps in separating different molecular species in a mixture, but as a form of unidirectional pumping such a system is not useful.

In Fig. 2(a) we plot flow profile results from four simulations with fixed frequency  $\omega/2\pi = 23.9$  GHz and varying amplitudes, exploring the range  $E = 7.89 \times 10^{-2} - 0.237$  V Å<sup>-1</sup>. The streaming velocity at the lowest amplitude (green curve) yields the lowest net flow rate, corresponding to a maximum velocity observable adjacent to the hydrophobic surface of approximately  $v_x = -20$  ms<sup>-1</sup>, similar to the previous case with  $E = 0.184$  V Å<sup>-1</sup> and  $\omega/2\pi = 6.69$  GHz. The red curve represents the case of the highest strength, achieving a maximum velocity of  $v_x = -80$  ms<sup>-1</sup>, again similar to the previous case  $E = 0.184$  V Å<sup>-1</sup> and  $\omega/2\pi = 41.1$  GHz, plotted in Fig. 1(a). The torque exerted on a water dipole, given by

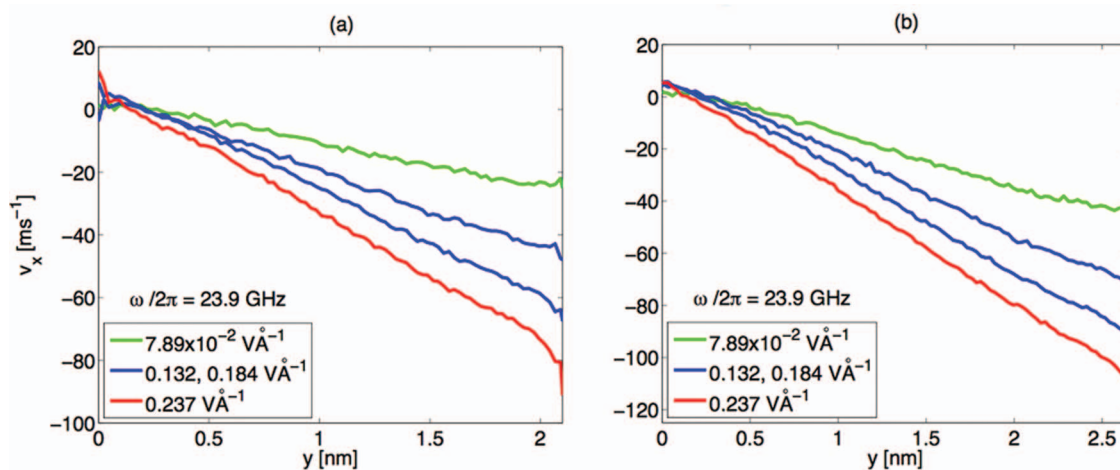


FIG. 2. Streaming velocity profiles across the channel of water confined between two different planar walls. (a) The width of the channel is  $h = 2.25$  nm. The frequency is kept constant while varying the amplitude. (b) As in (a), except for a larger channel width of  $h = 2.89$  nm. The hydrophilic surface is on the left, whereas the hydrophobic surface is on the right of both figures.

the term  $\boldsymbol{\mu} \times \mathbf{E}$ , provides a natural explanation of the trend observed in Fig. 2(a), namely that as the frequency is held constant, an increase in field amplitude results in greater torque on the water molecules, which in turn again increases the conversion of angular to linear momentum of the water molecules.

Next, we show the effect for a larger system size, depicted in Fig. 2(b), with water film thickness further increased to 2.9 nm. For consistency, we use the same field parameters as before, in this case  $\omega/2\pi = 23.9$  GHz and amplitude starting from  $E = 7.89 \times 10^{-2} \text{ V \AA}^{-1}$  to  $E = 0.237 \text{ V \AA}^{-1}$ . As expected, the lowest field amplitude  $E = 7.89 \times 10^{-2} \text{ V \AA}^{-1}$  (green curve) produces  $v_x = -40 \text{ ms}^{-1}$ , the lowest observed value. The maximum streaming velocity reaches the largest value  $v_x = -110 \text{ ms}^{-1}$  for  $E = 0.237 \text{ V \AA}^{-1}$  (red curve). Note that the slopes of Fig. 2(a) are lower than the corresponding slopes of Fig. 2(b). The potential difference inside the channel  $\Delta V$  increases if the spacing between the walls increases and the electric field is kept constant. As a consequence, the larger system of Fig. 2(b) experiences a larger potential than that of Fig. 2(a), and so more energy is pumped into the system. This observation opens up prospects for interesting benefits in experimental applications. Note that for almost all the simulation results, we observe a small non-zero slip velocity next to the hydrophilic surface. Only for the lowest electric field frequencies and strengths used (green lines) can the stick boundary condition assumption for the streaming velocity on the hydrophilic side be reproduced ( $v_x = 0 \text{ ms}^{-1}$ ), whereas a small deviation, compared with the hydrophobic side, can be detected as the frequency or the field strength increases. This result may appear controversial because it is usually assumed that the validity of the no-slip boundary condition at the hydrophilic solid surface holds (surface with a static contact angle less than  $90^\circ$ ), i.e. zero fluid velocity. But it has recently been found in simulations of Couette flow, that a liquid slip can occur on a hydrophilic solid surface,<sup>43</sup> which in our case is evident, to a different degree, in Figs. 1(a) (left side) and 1(b) (both sides).

In Fig. 3(a), we display the maximum streaming velocity as a function of electric field strength at a fixed frequency of 23.9 GHz for the  $h = 2.25$  nm system. Theory predicts that the streaming velocity should go as  $E^2$ ,<sup>15,18</sup> to lowest order in  $E$ . Indeed, we do see this quadratic dependence but only for relatively weak fields. As the field strength increases, the flow velocity flattens out and saturates at higher values as seen in Fig. 3(b), which is not predicted by existing theory. This saturation at higher fields suggests an optimal field strength for maximal flow throughput for any particular frequency. We note that for higher fields the polarizability of water depends on the magnitude of the electric field itself. This is not taken into account by the theory as it currently stands and hence it is unable to predict this flattening behaviour.

In like manner, the dependence of the maximum flow velocity on frequency for a variety of field strengths for the two different system sizes simulated is displayed in Figs. 3(c) and 3(d). For the larger system, we have  $N = 346$  water molecules, confined between two different surfaces  $h = 2.89$  nm apart. Bonthuis *et al.*<sup>18</sup> predict a frequency dependence that is linear at small frequencies and decays at higher frequencies. Our molecular dynamics data shows an almost linear increase for low frequencies, and a flattening of the maximum velocity at frequencies  $\gtrsim 100$  GHz. We also find that indeed the maximum velocity does decay in the frequency range  $150 \text{ GHz} \lesssim \nu \lesssim 1 \text{ THz}$  (not displayed). The frequencies required for this decay are very high, corresponding to time scales smaller than the dipolar relaxation time of water. Molecules do not have sufficient time to respond to the rotation of the field so their rotational motion is reduced, which in turn means that the coupling of rotational to linear momentum is progressively weaker as the frequency increases.

Our simulations also show that the flow rates can be increased by increasing the width of the channel (Fig. 3(d)), in qualitative agreement with theory,<sup>15,18</sup> though we note that it is not possible to find the actual (or approximate) functional dependence on channel width from only the two widths simulated in this work. Even though flow is in principle possible

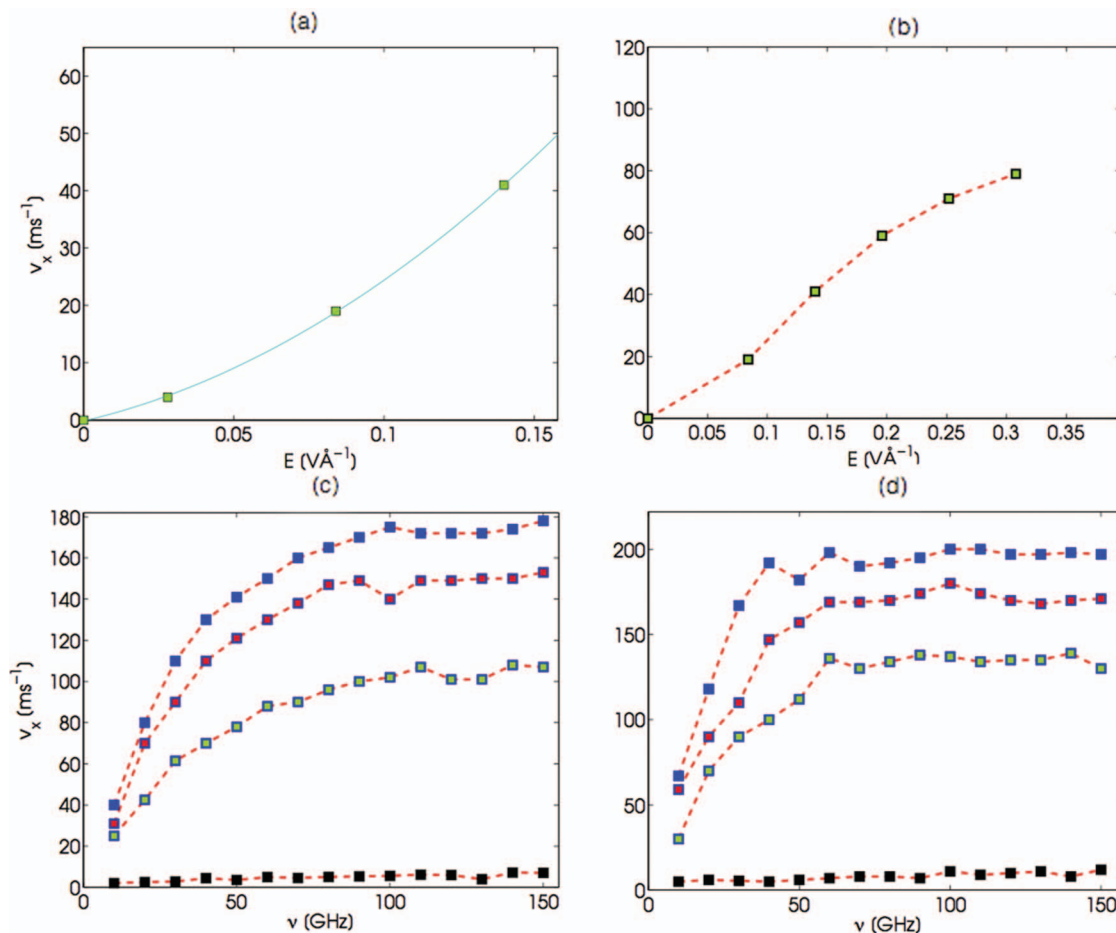


FIG. 3. (a) and (b) Maximum (absolute) streaming velocities adjacent to the hydrophobic wall versus electric field for  $h = 2.25$  nm and frequency 23.9 GHz. (a)  $0 \leq E < 0.15$   $\text{V}\text{\AA}^{-1}$ , with a quadratic fit (curve) and (b)  $0 \leq E < 0.35$   $\text{V}\text{\AA}^{-1}$  with points connected to guide the eye. (c) Maximum (absolute) streaming velocities versus electric field frequency for  $h = 2.25$  nm, (d) for  $h = 2.89$  nm. In (c), (d)  $E = 0.0289$   $\text{V}\text{\AA}^{-1}$  for the black colored squares, and 0.195, 0.363 and 0.531  $\text{V}\text{\AA}^{-1}$  for the green, red and blue squares, respectively. The field frequency ( $x$ -axis) ranges from 9.5 to 150 GHz.

at large channel widths, the physics dictates this would necessitate extremely large electrical potential differences to obtain the same field strength and/or frequencies, making the technique unfeasible for anything other than nano-scale flows.

In addition to illustrating how a rotating field can induce unidirectional flow of water, taking into account different boundary conditions, it is important to consider the effect of heating up the water, due to the dipolar loss mechanism.<sup>29,44,45</sup> We emphasize here that we are interested in finding not only the highest magnitudes for the velocity profiles, but, to some extent, maintaining the lowest fluid temperature. Excessive fluid heating could be detrimental for useful applications, particularly in systems involving manipulation of biomolecules. Unfortunately these two features are in competition, as we inevitably encounter a higher temperature when we tune the field parameters such as to optimize for higher net flow. Nonetheless, we will show that for certain frequencies and field amplitudes used in this study, both requirements can be satisfied.

Figure 4 shows the molecular temperature profile relative to Fig. 1(a), evaluated as

$$T_{mol} = \frac{1}{3Nk_B} \sum_i m_i \mathbf{c}_{i,cm}^2, \quad (9)$$

where  $N$  is the total number of water molecules and  $\mathbf{c}_{i,cm}$  is the *thermal* velocity of the center of mass of molecule  $i$  (i.e. the streaming centre of mass velocity is subtracted out). We restrict our analysis to the frequency range  $\omega/2\pi = 6.69 - 41.1$  GHz with fixed  $E = 0.184$   $\text{V}\text{\AA}^{-1}$ , as in Fig. 1(a). The smallest frequency,  $\omega/2\pi = 6.69$  GHz (colored in green), gives the lowest temperature  $T \approx 300$  K, which is equal to the wall temperature. Thus, no significant temperature increase throughout the fluid is observed for this lowest frequency, even though the corresponding  $v_x \approx -20$   $\text{ms}^{-1}$  remains a significant value. As the frequency rises, the temperature also gradually increases due to the excited reorientation of dipoles under the action of the external rotating field. When the frequency increases, molecular rotations also increase, resulting in an increase in temperature. The temperature profiles are maximum near the centre of the fluid and decrease monotonically towards their minimum values at the walls due to the conduction of heat from fluid to wall. Note that the profiles of Fig. 4 manifest a discontinuity in the temperature (so-called temperature jump) at the boundaries for higher frequencies (the walls are always maintained at a temperature of 300 K), which can be ascribed to the interfacial thermal resistance of the two walls.<sup>46</sup> These results confirm that a judicious choice of field strengths, frequency values and wall temperatures can

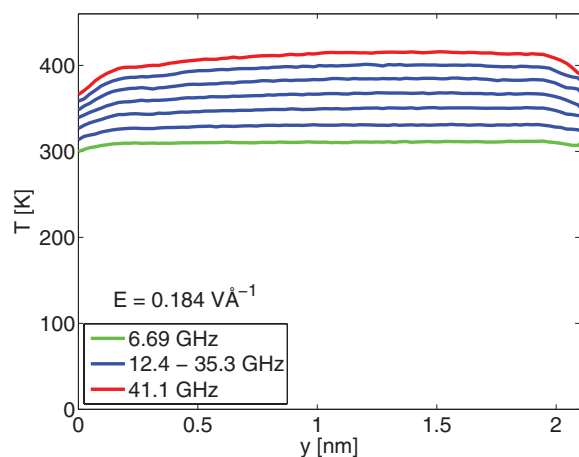


FIG. 4. Temperature profiles measured for fixed field strength  $E = 0.184 \text{ V \AA}^{-1}$  and frequency ranging from  $\omega/2\pi = 6.69 \text{ GHz}$  to  $41.1 \text{ GHz}$ .

generate significant non-zero net flow with moderate temperature increase within the fluid.

Our aim in this work is to convincingly demonstrate that unidirectional net flow can be induced for polar molecules in nanoconfined geometries. Our simulation results show qualitative agreement with theoretical predictions, but we can go one step further and demonstrate the quantitative accuracy of our simulations with our theoretical predictions. In order to do this, we compare our molecular dynamics results with the solutions of the extended Navier-Stokes equations (ENS), which include the effect of the intrinsic angular momentum.<sup>47–49</sup> For the geometry of Fig. 1, the ENS read in the low Reynolds number regime

$$\rho \frac{\partial u_x}{\partial t} = \rho F_e + (\eta_0 + \eta_r) \frac{\partial^2 u_x}{\partial y^2} - 2\eta_r \frac{\partial \Omega_z}{\partial y}, \quad (10)$$

$$\rho I \frac{\partial \Omega_z}{\partial t} = \rho \Gamma_z + 2\eta_r \left( \frac{\partial u_x}{\partial y} - 2\Omega_z \right) + \zeta \frac{\partial^2 \Omega_z}{\partial y^2}, \quad (11)$$

where  $\rho$  is the density,  $\eta_0$  and  $\eta_r$  are the shear and vortex viscosities, respectively, and  $\zeta = \zeta_0 + \zeta_r$  and  $I$  are the equivalent spin viscosities and the moment of inertia per unit mass of water. The external force in the  $x$ -direction acting on the molecules is  $F_e$  and  $\Gamma_z$  represents the external torque injected into the system by the external electric field.  $u_x$  is the streaming velocity in the direction parallel to the walls ( $x$ -direction),  $\Omega_z$  is the average molecular angular velocity field, describing rotation of the water molecules. Here we assume we can treat water as a uniaxial molecule, which is a reasonable approximation to make in order to solve the above coupled equations without the need for more complicated theoretical considerations.<sup>15</sup> We estimate the transport coefficients taking into consideration the fact that the temperature of the system used to compare with the numerical solution is approximately  $T = 380 \text{ K}$ . We set  $\eta_0 = 2.5 \times 10^{-4} \text{ Pa s}$ <sup>16</sup> and  $\zeta = 4.0 \times 10^{-22} \text{ kg ms}^{-1}$ , which has been treated as a free parameter since no estimate is available in the literature for this temperature. However, note that the two spin viscosities have been evaluated for the SPC/Fw water model in the range  $T = 284\text{--}319 \text{ K}$ ,<sup>15</sup> showing a decreasing tendency when the temperature increases, consistent with the free parameter es-

imate we use. The rotational viscosity has been estimated by solving Eq. (11) for  $\eta_r$  in the steady-state, i.e.,  $\partial \Omega_z / \partial t = 0$ , assuming  $\partial^2 \Omega_z / \partial y^2 = 0$ , for a lower field amplitude  $E = 0.094 \text{ V \AA}^{-1}$ . From the velocity profile for the amplitude  $E = 0.094 \text{ V \AA}^{-1}$  (not shown), we estimate  $\partial u_x / \partial y = 1.34 \times 10^{10} \text{ s}^{-1}$ . From the NEMD torque and angular velocity profiles (not shown) we estimate  $\Omega_z = 0.25 \times 10^{11} \text{ rad/s}$  and  $\Gamma_z = 15000 \text{ m}^2 \text{ s}^{-2}$ , giving  $\eta_r = 2.05 \times 10^{-4} \text{ Pa s}$  similar to  $\eta_r = 1.7 \times 10^{-4} \text{ Pa s}$ .<sup>15</sup> The density of water is  $\rho = 998 \text{ kg m}^{-3}$ . To estimate  $I$  we take the average of the three principal moments of inertia of SPC/E water, which gives  $I = 7.18 \times 10^{-22} \text{ m}^2$ . By choosing  $F_e = 0$  we assume that no external force (or pressure gradient) is present except the electric field, which enters the ENS by means of the torque term (see further discussion on the NEMD estimate of the torque profile).

Numerical solutions of the ENS compared with our molecular dynamics results are shown in Fig. 5 for the system  $E = 0.184 \text{ V \AA}^{-1}$  and  $\omega/2\pi = 23.9 \text{ GHz}$ . The ENS

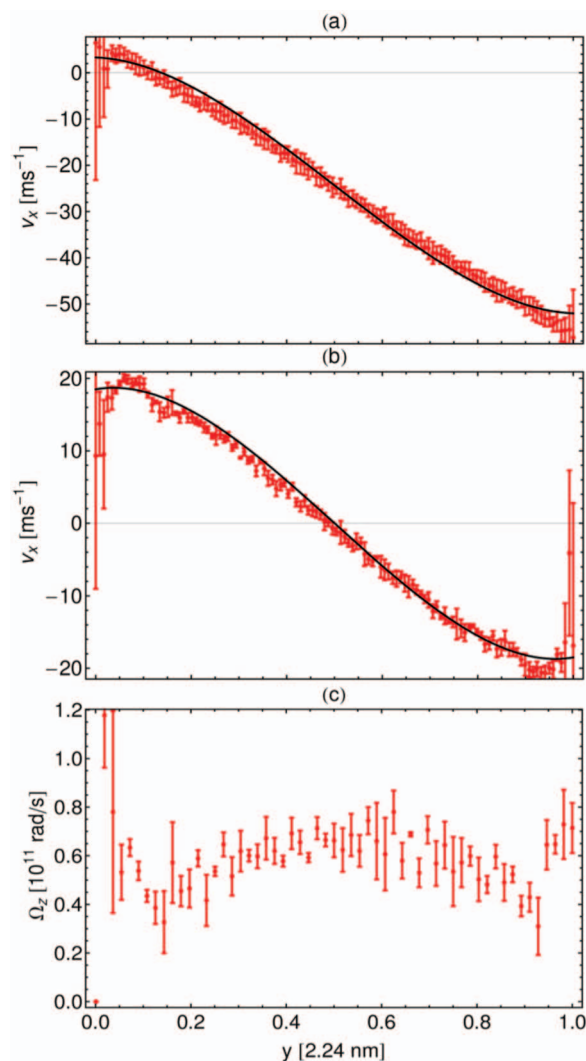


FIG. 5. Numerical solutions of the steady-state ENS. (a) Asymmetric channel ENS solution (solid black line), compared with NEMD simulation results (solid red circles) for  $E = 0.184 \text{ V \AA}^{-1}$  and  $\omega/2\pi = 23.9 \text{ GHz}$ . (b) Solution for the symmetric channel, compared with NEMD simulation results for the same field parameters. (c) NEMD data for the spin angular velocity. All error bars represent the associated standard deviations of six independent runs.

(Eqs. (10) and (11)) were solved using the Mathematica<sup>TM</sup> linear boundary value “chasing” (or “shooting”) solver. Agreement between the ENS linear velocity predictions and our NEMD data are excellent. Figure 5(a) shows the asymmetric channel ENS solution (solid black line), compared with NEMD simulation results (solid red circles) for  $E = 0.184 \text{ V \AA}^{-1}$  and  $\omega/2\pi = 23.9 \text{ GHz}$ . Data points and the associated standard deviations represent the averages of six independent runs, evaluated for each bin, for the system corresponding to the central, blue profile in Fig. 1(a). Slip boundary conditions are taken from molecular dynamics simulation data. On the left wall we have  $v_x(0) = 4 \text{ ms}^{-1}$  (approximately no slip boundary condition at the hydrophilic wall, compared with the hydrophobic wall) and on the right wall  $v_x(L) = -52 \text{ ms}^{-1}$ , where  $L = 2.2 \text{ nm}$  is the position of the hydrophobic wall. In Fig. 5(b) we present the solution for the symmetric channel, compared with NEMD simulation results for the same field parameters  $E = 0.184 \text{ V \AA}^{-1}$  and  $\omega/2\pi = 23.9 \text{ GHz}$ . Boundary conditions are again taken from the molecular dynamics simulations, with values  $v_x = \pm 18 \text{ ms}^{-1}$ . Note that due to the density depletion zones immediately adjacent

to both walls (and hence poor statistics), the width of the channel that is displayed is just 2.24 nm, and the  $x$  axis represents the  $y$ -position of the fluid normalised by this value. Finally, in Fig. 5(c) we show the NEMD data for the spin angular velocity. The corresponding numerical solution has not been depicted because the shape is not accurately captured. Nonetheless, by imposing in the numerical solver the boundary condition taken from the NEMD data, approximately  $\Omega_z = 0.7 \times 10^{11} \text{ rad/s}$  at both walls, the numerical average streaming angular velocity in the center of the channel is approximately the same as the NEMD profile. As we will see shortly, we can not assume the no-slip boundary conditions for the angular streaming velocities of water at both walls, i.e.,  $\Omega(0) = \Omega(L) \neq 0$ .

To quantify the term  $\Gamma_z$  in the right hand side of Eq. (11), we computed the specific torque (torque per unit mass) with the same binning technique used to evaluate the streaming velocity profile and then averaged over all water molecules. The water molecules' center of mass is positioned in a bin between  $y$  and  $y + \Delta y$  in the channel. Quantities are averaged over time and the final averaged torque per unit mass is computed at the end of the simulation, given by

$$\Gamma_z(y, t) = \frac{\langle \sum_i \sum_j ((x_{ij} - x_{i,cm})q_{ij}E_{iy}(t) - (y_{ij} - y_{i,cm})q_{ij}E_{ix}(t))\delta(y_i - y) \rangle}{\langle \sum_i m_i \delta(y_i - y) \rangle}, \quad (12)$$

where the first index  $i$  labels the water molecules and  $j$  indexes the three charged sites of the SPC/E model. The term  $x_{ij}$  represents the  $x$  coordinate position of site  $j$  of molecule  $i$  with respect to the simulation box reference frame. The term  $x_{i,cm}$  is the  $x$  component of the center of mass position of molecule  $i$ , expressed in the same coordinate system. The terms  $E_{ix}(t)$  and  $E_{iy}(t)$  describe the  $x$  and  $y$  components of the external electric field, and  $q_{ij}$  is the charge of site  $j$  of molecule  $i$ . The result is shown in Fig. 6, from which we use a value near the centre of the channel of  $\Gamma_z = 20000 \text{ m}^2 \text{ s}^{-2}$  to be inserted in Eq. (11).

We solve the dimensionless form of the associated steady-state problem of the ENS (Eqs. (10) and (11)), taking zero for the time-derivative terms and rescaling the dynamical variables with  $L_0 = 2.2 \text{ nm}$ , the width of the channel, and  $u_0 = 10 \text{ ms}^{-1}$ , a value comparable to results from NEMD simulations. Boundary conditions at the walls for  $u_x$ , as explained, are input into the numerical solution using those values determined directly from the apparent slip velocities obtained from the NEMD data.

In order to compare our numerical velocity profiles to the actual molecular dynamics data, we also need to compute the spin angular velocity from our molecular dynamics simulations. We do this as follows. The streaming angular velocity profile can be estimated from  $\mathbf{S} = \mathbf{\Theta} \cdot \mathbf{\Omega}$ ,<sup>38,39</sup> in which  $\mathbf{S}$ ,  $\mathbf{\Theta}$ , and  $\mathbf{\Omega}$  are the specific spin angular momentum vector,

moment of inertia tensor and the streaming angular velocity vector, respectively. The intrinsic angular momentum vector for a single water molecule is calculated by

$$\mathbf{S}_j = \sum_i (\mathbf{r}_{ji} - \mathbf{r}_{j,cm}) \times m_i (\mathbf{v}_{ji} - \mathbf{v}_{j,cm}), \quad (13)$$

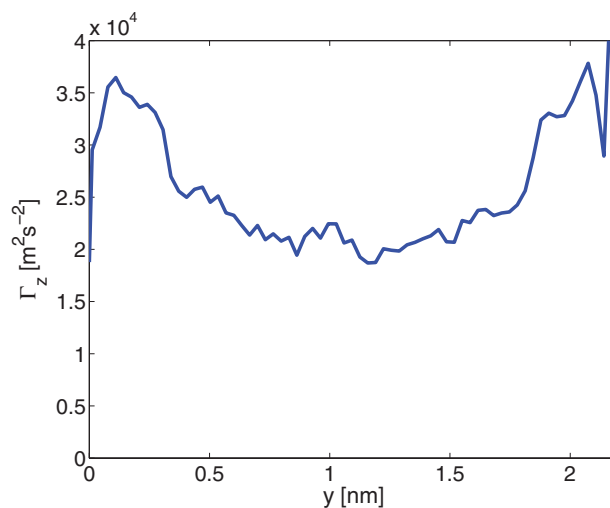


FIG. 6.  $z$ -component profile of the torque per unit water mass, computed from Eq. (12) for the system with  $N = 270$  water molecules. The torque is injected by the uniform rotating field with  $E = 0.184 \text{ V \AA}^{-1}$  and  $\omega/2\pi = 23.9 \text{ GHz}$ .

where  $\mathbf{r}_{ji}$  and  $\mathbf{v}_{ji}$  are the positions and velocities of the three  $i$  sites of the  $j$  molecule, evaluated with respect to the simulation box reference frame, with  $\mathbf{r}_{j,cm}$  and  $\mathbf{v}_{j,cm}$  being the center of mass position and the center of mass velocity, and  $m_i$  the mass of the hydrogen and oxygen sites.

With the same binning technique described earlier, every 10 time steps we compute the specific spin angular momentum

$$\mathbf{S}(y, t) = \frac{\langle \sum_j \mathbf{S}_j(y, t) \delta(y_j - y_{j,cm}) \rangle}{\langle \sum_j m_j \delta(y_j - y_{j,cm}) \rangle} \quad (14)$$

and the specific moment of inertia

$$\Theta(y, t) = \frac{\langle \sum_j \Theta_j(y, t) \delta(y_j - y_{j,cm}) \rangle}{\langle \sum_j m_j \delta(y_j - y_{j,cm}) \rangle} \quad (15)$$

where the index  $j$  spans over all the water molecules with center of mass located in the bin between the distance  $y_i$  and  $y_i + \Delta_i$  across the channel and the angle brackets again refer to the time average. At the end of the simulation, for every bin, we solve the linear system  $\mathbf{S} = \Theta \cdot \Omega$  for  $\Omega$ , obtaining a profile for the streaming angular velocity across the channel ( $y$ -direction).<sup>38,39</sup> Our method was tested for accuracy in a standard steady-state Poiseuille flow NEMD simulation (flow in the  $x$ -direction with confinement in the  $y$ -direction), in which it is known that the angular velocity for a sufficiently wide channel (where spin diffusion can be ignored) goes as  $\Omega_z = -\dot{\gamma}/2$ , where  $\dot{\gamma}$  is the strain rate, and this was indeed verified.

To ensure that the channel width was wide enough, we plot the number density against channel position in Fig. 7, evaluated with the external field off. No significant density oscillations are detectable in the center of the channel. In Fig. 7 it is also recognizable that the first peak on the left, corresponding to the hydrophilic surface, results in molecules slightly shifted towards the wall and more tightly packed than the corresponding peak on the hydrophobic wall (right side of the figure). This suggests a larger wetting of the left surface due to the additional charges placed on the wall. On the opposite side, the repulsion of water molecules by the hydrophobic

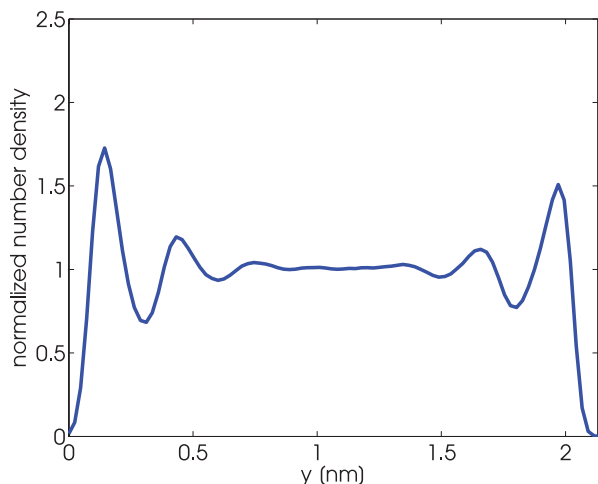


FIG. 7. Number density profile of water as a function of the distance from the hydrophilic plate (on the left).

wall is partly imposed by the WCA potential, which has no attractive part, and partly by its higher density.

The other significant point to note about the angular velocity profile is that a naive assumption of zero spin angular velocity at the walls (i.e., no-slip angular velocity boundary condition) leads to a severe mismatch between the numerical solution and the NEMD results. We have thus used the measured NEMD slip angular velocity at both walls as the boundary conditions for the solution of the ENS equation. In this sense, our numerical approach in solving the ENS, which at first sight appears simpler than a fully analytical treatment, is in fact revealing the importance of a correct choice of the boundary conditions for the velocity and angular velocity profiles, which in turn may not be accurately estimated without resorting to NEMD results.

We also draw attention to the fact that the external electric field acting on the sites of water, which enters the Newtonian equations of motion, Eq. (5), should be interpreted as an effective electric field, implying that the real external field is the effective field multiplied by the permittivity of the particular fluid system under investigation.

Finally, we attempted to compare our NEMD simulation data for the streaming velocity profiles with the predictions of Bonthuis *et al.*<sup>18,19</sup> at relatively low field and frequency of  $E = 0.094 \text{ V \AA}^{-1}$  and  $\omega/2\pi = 23.9 \text{ GHz}$ . While we found qualitative agreement between the shape of the predicted profiles and the actual NEMD data, quantitative agreement was not that good. In fact, for our field strength (roughly an order of magnitude larger than that used by Bonthuis *et al.*<sup>19</sup> in their estimation of the dipolar relaxation time and polarizability per unit mass used in their theory) we find a dipolar relaxation time of 2 ps, which is significantly lower than the value of  $7 \pm 2 \text{ ps}$  used by them. In order to quantitatively find better agreement with their analytic theory we would need to conduct our simulations at an order of magnitude lower field strength, which unfortunately would result in poor statistical accuracy for the system size we are working with. This in fact demonstrates the robustness of the numerical approach taken by us in solving Eqs. (10) and (11), in that it is more applicable at higher field strengths compared to the existing analytic treatment which is only strictly valid at lower fields.

## IV. CONCLUSION

We have conducted the first computer experiment to convincingly demonstrate that coupling of spin angular momentum to linear streaming momentum of a polarizable liquid such as water can be exploited to generate sustained and non-intrusive pumping for nanofluidic devices. Such a pumping mechanism obviates the need for any form of intrusive mechanical forcing or electronic circuitry to generate potential differences. Our numerical experiments confirm up to a point previous theoretical predictions, but also importantly highlight limitations to them. Equally importantly, we demonstrate how flow can be achieved under laboratory conditions in which a rotating field acts upon a nanofluidic water system such that its symmetry is broken by a judicious choice of hydrophobic and hydrophilic channel walls. Under such conditions a net non-zero unidirectional and non-negligible

flow of water is generated. We find that higher field strengths and/or higher frequencies generate stronger flows, up to a finite saturation level. Our simulation results are used to verify the extended Navier-Stokes equations incorporating intrinsic molecular spin and its associated transport coefficients. The effect of the heating on the system was also investigated and we find that a significant flow rate can be induced without the water temperature increasing by any significant amount. This has important implications for nanofluidic devices such as lab-on-a-chip detectors that are sensitive to the effects of high temperature on biomolecules. Further studies to follow will investigate wall materials such as graphene (hydrophobic) and functionalised silica (hydrophilic) as feasible materials for laboratory based experiments to be undertaken.

## ACKNOWLEDGMENTS

Computational resources were provided by the Swinburne Supercomputer Centre, the Victorian Partnership for Advanced Computing HPC Facility and Support Services and an award under the Merit Allocation Scheme on the NCI National Facility at the Australian National University. J.S.H. wishes to acknowledge Lundbeckfonden for supporting this work as a part of Grant No. R49-A5634. We also thank one of the referees for very useful suggestions that have improved the manuscript.

- <sup>1</sup>J. C. T. Eijkel and A. van den Berg, *Microfluid. Nanofluid.* **1**, 249 (2005).
- <sup>2</sup>M. Napoli, J. C. T. Eijkel, and S. Pennathur, *Lab Chip* **10**, 957 (2010).
- <sup>3</sup>W. Sparrebroom, A. van den Berg, and J. C. T. Eijkel, *New J. Physics* **12**, 015004 (2010).
- <sup>4</sup>H. Bruus, *Theoretical Microfluidics* (Oxford University Press, Oxford, 2008).
- <sup>5</sup>D. M. Huang, C.-B. Cecile, Y. Christophe, and L. Bocquet, *Phys. Rev. Lett.* **98**, 177801 (2007).
- <sup>6</sup>B. J. Kirby, *Micro- and Nanoscale Fluid Mechanics: Transport in Microfluidic Devices* (Cambridge University Press, Cambridge, 2010).
- <sup>7</sup>H. Ouyang, X. Zhenhai, and J. Zhe, *Microfluid. Nanofluid.* **9**, 915 (2010).
- <sup>8</sup>P. Dutta and J. Morse, *Recent Pat. Nanotechnol.* **2**, 150 (2008).
- <sup>9</sup>H. Li, L. E. Ocola, O. Auciello, and M. Firestone, *J. Vac. Sci. Technol. A* **26**, 752 (2008).
- <sup>10</sup>H. Liu, S. Dharmatilleke, and A. A. O. Tay, *Microsyst. Technol.* **16**, 561 (2010).
- <sup>11</sup>N. G. Green, A. Ramoz, A. Gonzalez, H. Morgan, and A. Castellanos, *Phys. Rev. E* **66**, 026305 (2002).
- <sup>12</sup>N. R. Tas, J. W. Berenschot, T. S. Lammerink, M. Elwenspoek, and A. van den Berg, *Anal. Chem.* **74**, 2224 (2002).
- <sup>13</sup>M. Barbic and A. Scherer, *Solid State Nucl. Magn. Reson.* **28**, 91 (2005).
- <sup>14</sup>K. F. Rinne, S. Gekle, D. J. Bonthuis, and R. R. Netz, *Nano Lett.* **12**, 1780 (2012).
- <sup>15</sup>J. S. Hansen, H. Bruus, B. D. Todd, and P. J. Daivis, *J. Chem. Phys.* **133**, 144906 (2010).
- <sup>16</sup>A. P. Markesteijn, R. Hartkamp, S. Luding, and J. Westerweel, *J. Chem. Phys.* **136**, 134104 (2012).
- <sup>17</sup>J. S. Hansen, J. C. Dyre, P. J. Daivis, B. D. Todd, and H. Bruus, *Phys. Rev. E* **84**, 036311 (2011).
- <sup>18</sup>D. J. Bonthuis, D. Horinek, L. Bocquet, and R. R. Netz, *Phys. Rev. Lett.* **103**, 144503 (2009).
- <sup>19</sup>D. J. Bonthuis, D. Horinek, L. Bocquet, and R. R. Netz, *Langmuir* **26**, 12614 (2010).
- <sup>20</sup>B. U. Felderhof, *Phys. Fluids* **23**, 092002 (2011).
- <sup>21</sup>J. S. Hansen, P. J. Daivis, and B. D. Todd, *Microfluid. Nanofluid.* **6**, 785 (2009).
- <sup>22</sup>J. S. Hansen, B. D. Todd, and P. J. Daivis, *Phys. Rev. E* **80**, 046322 (2009).
- <sup>23</sup>J. S. Hansen, B. D. Todd, and P. J. Daivis, *Phys. Rev. E* **84**, 016313 (2011).
- <sup>24</sup>M. Born, *Z. Phys.* **1**, 221 (1920).
- <sup>25</sup>H. J. C. Berendsen, J. R. Grigera, and T. P. Straatsma, *J. Phys. Chem.* **91**, 6269 (1987).
- <sup>26</sup>M. A. Gonzalez and J. L. F. Abascal, *J. Chem. Phys.* **132**, 096101 (2010).
- <sup>27</sup>G. Ciccotti, M. Ferrario, and J. P. Ryckaert, *Mol. Phys.* **47**, 1253 (1982).
- <sup>28</sup>Y. S. Badyal, M.-L. Saboungi, D. L. Price, S. D. Shastri, D. R. Haefner, and A. K. Soper, *J. Chem. Phys.* **112**, 9206 (2000).
- <sup>29</sup>N. J. English and J. M. D. MacElroy, *J. Chem. Phys.* **118**, 1589 (2003).
- <sup>30</sup>J. D. Weeks, D. Chandler, and H. C. Andersen, *J. Chem. Phys.* **54**, 5237 (1971).
- <sup>31</sup>D. Wolf, P. Keblinski, S. R. Phillpot, and J. Eggebrecht, *J. Chem. Phys.* **110**, 8254 (1999).
- <sup>32</sup>K. Takahashi, T. Narumi, and K. Yasuoka, *J. Chem. Phys.* **134**, 174112 (2011).
- <sup>33</sup>D. Rapaport, *The Art of Molecular Dynamics Simulation*, 2nd ed. (Cambridge University Press, New York, 2004).
- <sup>34</sup>S. Nosé, *J. Chem. Phys.* **81**, 511 (1984).
- <sup>35</sup>S. Nosé, *Mol. Phys.* **52**, 255 (1984).
- <sup>36</sup>W. G. Hoover, *Phys. Rev. A* **31**, 1695 (1985).
- <sup>37</sup>S. Bernardi, B. D. Todd, and D. J. Searles, *J. Chem. Phys.* **132**, 244706 (2010).
- <sup>38</sup>K. P. Travis, P. J. Daivis, and D. J. Evans, *J. Chem. Phys.* **103**, 1109 (1995).
- <sup>39</sup>K. P. Travis, P. J. Daivis, and D. J. Evans, *J. Chem. Phys.* **103**, 10638 (1995).
- <sup>40</sup>K. P. Travis, P. J. Daivis, and D. J. Evans, *J. Chem. Phys.* **105**, 3893 (1996).
- <sup>41</sup>N. Asproulis and D. Drikakis, *Phys. Rev. E* **81**, 061503 (2010).
- <sup>42</sup>M. P. Allen and D. J. Tildesley, *Computer Simulation of Liquids* (Clarendon Press, Oxford, 1987).
- <sup>43</sup>T. A. Ho, D. V. Papavassiliou, L. L. Lee, and A. Striolo, *Proc. Natl. Acad. Sci. U.S.A.* **108**, 16170 (2011).
- <sup>44</sup>A. C. Metaxas and R. J. Meredith, *Industrial Microwave Heating* (Peter Peregrinus Ltd, London, 1983).
- <sup>45</sup>M. Tanaka and M. Sato, *J. Chem. Phys.* **126**, 034509 (2007).
- <sup>46</sup>R. Khare, P. Keblinski, and A. Yethiraj, *Int. J. Heat Mass Transfer* **49**, 3401 (2006).
- <sup>47</sup>D. J. Evans and W. B. Streett, *Mol. Phys.* **36**, 161 (1978).
- <sup>48</sup>S. R. de Groot and P. Mazur, *Non-Equilibrium Thermodynamics* (Dover, Mineola, 1984).
- <sup>49</sup>D. W. Condiff and J. S. Dahler, *Phys. Fluids* **7**, 842 (1964).
- <sup>50</sup>W. Humphrey, A. Dalke, and K. Schulten, *J. Mol. Graphics* **14**, 33 (1996).